



Paper Type: Original Article



Layerwise Finite Element Approach for the Bending Analysis of Bi-Directional Functionally Graded Layered Plates

Laith O. Mazahreh^{1,*} , Ibrahim Mousa Abu-Alshaikh² 

¹ Oil and Natural Gas Directorate, Ministry of Energy and Mineral Resources, Amman, Jordan; laith_mazahreh@hotmail.com;

¹ Department of Mechanical Engineering, Faculty of Engineering, University of Jordan, Amman, Jordan; laith_mazahreh@hotmail.com;

² Department of Mechanical Engineering, University of Jordan, Amman-11942, Jordan; i.abualshaikh@ju.edu.jo.

Citation:



Mazahreh, L. O., & Abu-Alshaikh, I. M. (2021). Layerwise finite element approach for the bending analysis of bi-directional functionally graded layered plates. *Journal of applied research on industrial engineering*, 8(2), 176-194.

Received: 06/02/2021

Reviewed: 01/04/2021

Revised: 30/04/2021

Accept: 12/05/2021

Abstract

In this paper, layerwise finite element analysis for the bending behavior of two-dimensional functionally graded layered plates with different boundary conditions is presented. The plates consist of three layers; a functionally graded layer embedded between ceramic and metal isotropic layers. The layerwise approach is based on the third-order shear deformation theory for the middle layer, while the first-order shear deformation theory is used for both the upper and lower isotropic layers. A quadrilateral 8-noded element with 13-degrees of freedom per node is used for this purpose. The present results show very good agreements with the published results for similar problems in literature solved by other methods of plates consist of either single or layered functionally graded plates.

Keywords: Two-dimensional functionally graded materials, Bending, Plates, Higher-order, Layerwise, Finite element.

1 | Introduction

Cracking and delamination, which are often observed in conventional multilayer composite materials, are one of the major observed drawbacks comparing to Functionally Graded Materials (FGM). FGM were discovered back in 1984 were a group of material scientists in the Sendai area of Japan introduced the concept of a new type of material named it as functionally gradient material as a means of preparing thermal barrier materials materials [1]. Since then, the use of FGM in a wide range of applications has been introduced especially in the fields of biomaterials serving as an artificial bone in the human body and aeronautics [2].

 Licensee Journal of Applied Research on Industrial Engineering. This article is an open access article distributed under the terms and conditions of the Creative Commons Attribution (CC BY) license (<http://creativecommons.org/licenses/by/4.0>).

To study FGM structure behavior, wide ranges of 2D theories are applied such as the Classical Plate Theory (CPT), First-order Shear Deformation Theory (FSDT), Higher-order Shear Deformation Theory (HSDT), Zig-Zag and layerwise approach. Irfan [3] conducted a comprehensive overview of the recent research trends in Finite Element (FE) formulations for analyzing sandwich plates carried out since 2000. Various theories that are based on FSDT, HSDT, mixed solid-shell elements, Zig-Zag and global-local theories were presented. They concluded that a major portion of research efforts are being employed to develop the FE formulations based on different HSDT rather than Zig-Zag theories since large computational efforts are needed to develop the later approach comparing to the former one.

The FSDT theory, which assumes a constant shear strain value throughout the thickness of the plate, was widely used in literature. Khorramabadi et al. [4] studied analytically the effect of using FSDT and TSDT on the free vibrational behavior of FGM plates using Navier's solution method. Singha et al. [5] studied the nonlinear behaviors FGM plates under transverse distributed load using plate-bending FE. The resultant error from using FSDT encouraged researches to use HSDT, especially when dealing with thick plates. Moita et al. [6] studied using FE approach the linear and nonlinear static behavior of FGM plate shell structures using TSDT. The FE models were based on a non-conforming triangular flat plate shell element with 3-nodes and either 8 or 11-Degrees of Freedom (DoF) per node. Čukanović et al. [7] proposed a new shape function containing hyperbolic cosine function to study bending analysis of thick and moderately thick square and rectangular plates as well as plates on Winkler–Pasternak elastic foundation subjected to a sinusoidal transverse load. Efraim [8] derived an empirical accurate correlation formula between the frequencies of FGM plates and the constituent materials. Thang et al. [9] investigated the non-linear static analysis of thin curved panels with FG coatings under combined axial compression and external pressure using the classical shell theory. Nguyen et al. [10] analyzed non-uniform polygonal cross-sections for thin-walled FG straight and curved beams using higher order approach. Lezgy-Nazargah et al. [11] studied the static, free vibration and dynamic response of FG piezoelectric material beams using an efficient three-nodded beam element.

In general, the layerwise approach is introduced to ensure the continuity of the displacement fields across the interfaces of composite and FGM layered plates. Yas et al. [12] applied layerwise FE formulations to analyze FGM cylindrical shells with finite length subjected to dynamic load. Pandey and Pradyumna [13] also used a layerwise approach based on the assumption of the FSDT theory in each layer imposing continuity of displacements at each layer's interface. Nikbakht et al. [14] used the full layerwise method to analyze the elastic bending of FG plates up to yielding.

Many other types of research have used available commercial software such as ABAQUS, MATLAB and Maple to study the behavior of FGM plates. Kurtaran [15] published an article studying the effect of the plate's shape on the vibration and modal analysis for FGM plates using MATLAB software. Martínez-Pañeda [16] used ABAQUS software to analyze stresses of FGM plate using two schemes: nodal based gradation and Gauss integration point-based gradation. Al-Hawamdeh et al. [17] used the Maple software program to study the static behavior of a layered beam structure made of FGM material embedded between metal and ceramic layers.

Applications of FGM may require the variation of mechanical properties to be in more than one direction, i.e., 2D-FGM. A 2D-FGM may consist of more than two constituent materials where usually 2D-FGM outperforms ordinary FGM. Hedia [18] conducted a comparison study between both 1D-FGM and 2D-FGM for the backing shell of the cemented acetabular cup. Nemat-Alla [19] made a comparison study between 1D-FGM and 2D-FGM plates under super high temperatures using the FE approach where his work indicated that 2D-FGM had high capabilities to reduce thermal and residual stresses more efficiently comparing to conventional FGM. Similar to 1D-FGM, 2D-FGM may be analyzed using any of the previously discussed theories. Joshi and Kar [20] recently studied the bending behavior of 2D-FGM using FE approach that was developed using the APDL platform. Asemi et al. [21] investigated the static analysis of 2D-FGM plates based on the 3D theory of elasticity. Nguyen and Lee [22] analyzed flexural-torsional vibration and buckling of thin-walled 2D-FG beams with different cross sections. Nguyen and Lee [23]

also investigated the static behaviors and interactive geometric interpretation for modeling of thin-walled 2D-FGM beams using Vlasov’s theory. Lezgy-Nazargah [24] analyzed fully coupled thermo-mechanical 2D-FGM beams using NURBS FE. Lezgy-Nazargah and Meshkani [25] also studied the static and free vibration analyses of FGM plates rested on two-parameter elastic foundations using mixed FE approach.

Although many research areas regarding the FGM plates have been already covered, none of the research areas in literature covered the part of analyzing 2D-FG layered plates using the layerwise FE approach. In this paper, the layerwise FE methods will be used to investigate the bending behavior of a 2D-FG layer embedded between ceramic and metal isotropic layers with both TSDT for the 2D-FG layer and FSDT for the isotropic layers. Furthermore, special case studies of the aforementioned plate problems will be investigated and compared with the existing literature.

2 | Mathematical Model

The model under study consists of a 2D-FGM embedded between homogenous materials (metal and ceramic). The middle layer consists of a 2D-FGM that contains four distinct material constituents, two ceramics C_1 and C_2 at its upper surface and two metals M_1 and M_2 at its lower surface. Plate geometry involves mainly individual layer thicknesses h_1 , h_2 and h_3 for the bottom, middle and upper layers, respectively, besides, plate’s length and width represented by a and b , respectively, *Fig. 1*.

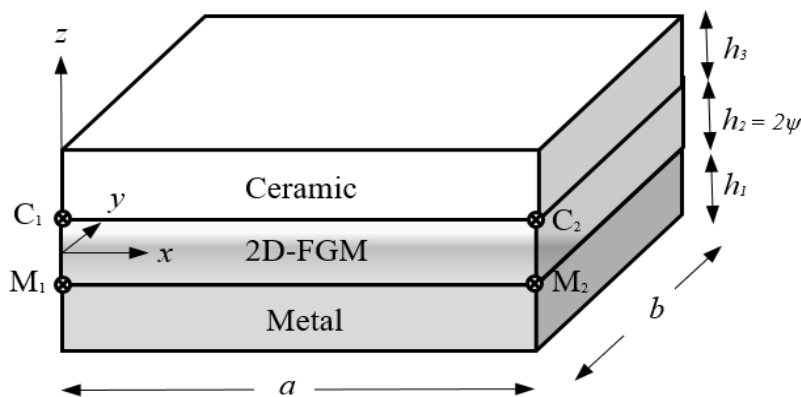


Fig. 1. Geometry of the 2D-FGM layered plate.

The variation of the volume fraction distribution for each material in the 2D-FG layer can be written as [21].

$$V_{C_1} = \left(1 - \left(\frac{x}{a} \right)^{n_x} \right) \left(\frac{z}{h_2} + \frac{1}{2} \right)^{n_z} . \tag{1}$$

$$V_{C_2} = \left(\frac{x}{a} \right)^{n_x} \left(\frac{z}{h_2} + \frac{1}{2} \right)^{n_z} . \tag{2}$$

$$V_{M_1} = \left(1 - \left(\frac{x}{a} \right)^{n_x} \right) \left(1 - \left(\frac{z}{h_2} + \frac{1}{2} \right)^{n_z} \right) . \tag{3}$$

$$V_{M_2} = \left(\frac{x}{a} \right)^{n_x} \left(1 - \left(\frac{z}{h_2} + \frac{1}{2} \right)^{n_z} \right) . \tag{4}$$

Where n_x and n_z are non-zero parameters known as volume fraction exponents. These exponents represent constituent distributions in x and z -directions. V_{C_1} , V_{C_2} , V_{M_1} and V_{M_2} are the volume fractions of the material constituents C_1 , C_2 , M_1 and M_2 , respectively. Fig. 2 and Fig. 3 represent the through-thickness and the through-width volume fraction variations for different values of n_z and n_x .

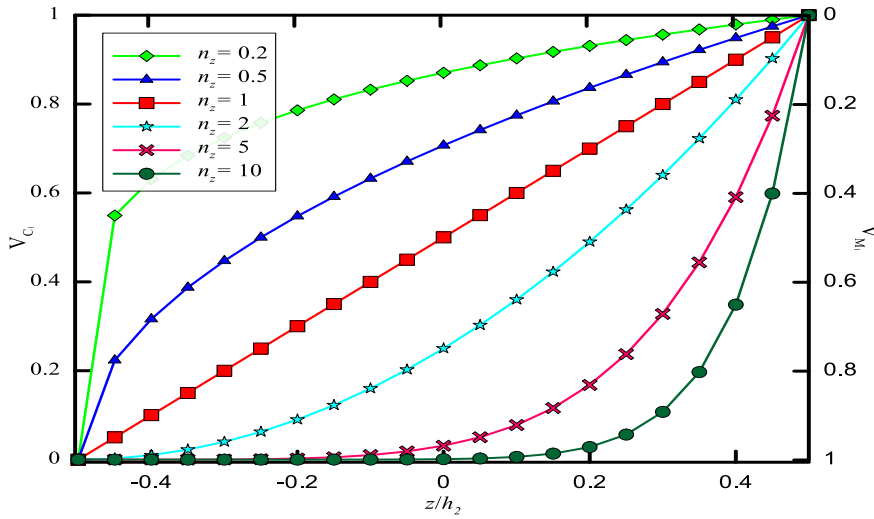


Fig. 2. Through-thickness volume fraction variation of both m_1 and c_1 material constituents for different values of n_z and a value of zero for n_x .

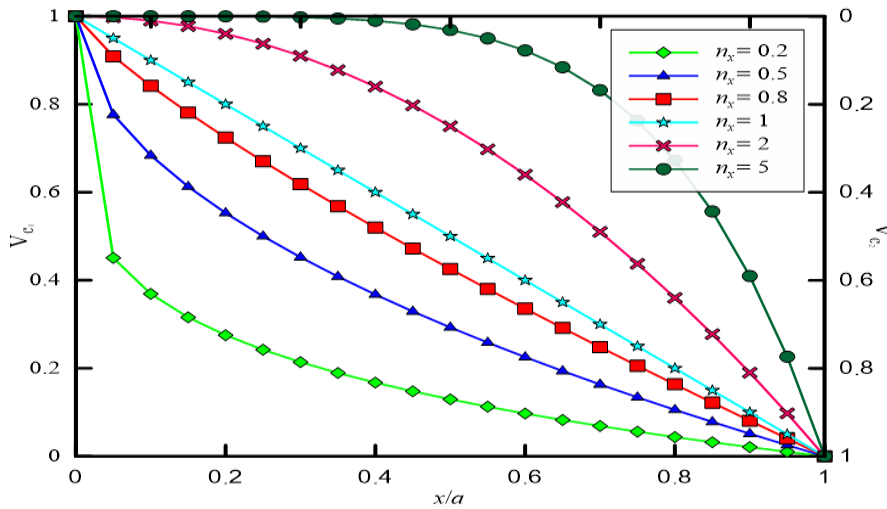


Fig. 2. Through-width volume fraction variation of both c_1 and c_2 material constituents for different values of n_x and a value of zero for n_z .

Material properties such as modulus of elasticity E at any arbitrary point (x, z) in the 2D-FG layer can be determined by a linear combination of volume fractions multiplied by the material property for each constituent material [13].

$$E(x, z) = E_{C_1} V_{C_1} + E_{C_2} V_{C_2} + E_{M_1} V_{M_1} + E_{M_2} V_{M_2} \quad (5)$$

where E_{C_1} , E_{C_2} , E_{M_1} and E_{M_2} are the moduli of elasticity for material constituents C_1 , C_2 , M_1 and M_2 , respectively. In the present study, a combination of FSDT and TSDT will be used to assign the displacement fields for the FGM structure embedded between two isotropic homogenous layers, where the use of higher order displacement fields such as TSDT results in a higher DoF comparing to lower order displacement fields such as FSDT. The displacement fields for the three layers of the plate shown in Fig. 1 can be expressed as

$$\begin{aligned}
 u^{(1)}(x, y, z) &= u_o + z^{(1)}\theta_x^{(1)}, \\
 v^{(1)}(x, y, z) &= v_o + z^{(1)}\theta_y^{(1)}, \\
 w^{(1)}(x, y, z) &= w_o.
 \end{aligned} \tag{6}$$

$$\begin{aligned}
 u^{(2)}(x, y, z) &= u_o + z^{(2)}\theta_x^{(2)} + (z^{(2)})^2 u^* + (z^{(2)})^3 \theta_x^*, \\
 v^{(2)}(x, y, z) &= v_o + z^{(2)}\theta_y^{(2)} + (z^{(2)})^2 v^* + (z^{(2)})^3 \theta_y^*, \\
 w^{(2)}(x, y, z) &= w_o.
 \end{aligned} \tag{7}$$

$$\begin{aligned}
 u^{(3)}(x, y, z) &= u_o + z^{(3)}\theta_x^{(3)}, \\
 v^{(3)}(x, y, z) &= v_o + z^{(3)}\theta_y^{(3)}, \\
 w^{(3)}(x, y, z) &= w_o.
 \end{aligned} \tag{8}$$

The TSDT is assigned for the middle 2D-FG layer, Eq. (7), whereas FSDT is assigned for both the top and bottom layers of the plate. In Eqs. (6-8), u_o , v_o and w_o are the displacements of mid-plane along x , y and z -directions, θ_x and θ_y are the rotations of normal to mid-plane about the y and x -axes, respectively, u^* , v^* , θ_x^* and θ_y^* are the coefficients of the higher-order terms in Taylor's series expansion of the displacement fields of the middle layer. Superscripts 1, 2 and 3 inside parentheses indicate the layer's number assigned in ascending order, i.e., the bottom layer is assigned by layer 1 whereas the upper layer is assigned by layer 3. To maintain the continuity conditions at the layer interfaces, the layerwise approach should be included in the displacement field equations for both the upper and lower layers. Thus, the conditions needed to modify the displacement field equations at the interfaces between layers 1-2 and layers 2-3, can be written as

$$\begin{aligned}
 u^{(1)}(x, y, -\psi) &= u^{(2)}(x, y, -\psi), \quad v^{(1)}(x, y, -\psi) = v^{(2)}(x, y, -\psi), \\
 u^{(3)}(x, y, \psi) &= u^{(2)}(x, y, \psi), \quad v^{(3)}(x, y, \psi) = v^{(2)}(x, y, \psi).
 \end{aligned} \tag{9}$$

where ψ is the half-thickness of the middle layer, i.e., $\psi = h_2 / 2$. Using Eqs. (6)-(9), the modified displacement field equations for both the upper and lower layers are obtained as [26]:

$$\begin{aligned}
 u^{(1)}(x, y, z) &= u^{(2)}(x, y, -\psi) + (z + \psi)\theta_x^{(1)} \\
 &= u_o - \psi\theta_x^{(2)} + \psi^2 u^* - \psi^3 \theta_x^* + (z + \psi)\theta_x^{(1)}. \\
 v^{(1)}(x, y, z) &= v^{(2)}(x, y, -\psi) + (z + \psi)\theta_y^{(1)} \\
 &= v_o - \psi\theta_y^{(2)} + \psi^2 v^* - \psi^3 \theta_y^* + (z + \psi)\theta_y^{(1)}.
 \end{aligned} \tag{10}$$

$$\begin{aligned}
 u^{(3)}(x, y, z) &= u^{(2)}(x, y, \psi) + (z - \psi)\theta_x^{(3)} \\
 &= u_o + \psi\theta_x^{(2)} + \psi^2 u^* + \psi^3 \theta_x^* + (z - \psi)\theta_x^{(3)}. \\
 v^{(3)}(x, y, z) &= v^{(2)}(x, y, \psi) + (z - \psi)\theta_y^{(3)} \\
 &= v_o + \psi\theta_y^{(2)} + \psi^2 v^* + \psi^3 \theta_y^* + (z - \psi)\theta_y^{(3)}.
 \end{aligned} \tag{11}$$

Proceeding further deriving the strain-displacement relations including both normal and shear strains (ε and γ). Strains are simply the partial derivatives of displacement fields with respect to x or y or a combination of both which are stated for each layer as:

$$\begin{aligned}
 \epsilon_{xx}^{(1)} &= \frac{\partial u^{(1)}}{\partial x} = \frac{\partial u_o}{\partial x} - \psi \frac{\partial \theta_x^{(2)}}{\partial x} + \psi^2 \frac{\partial u^*}{\partial x} - \psi^3 \frac{\partial \theta_x^*}{\partial x} + (z + \psi) \frac{\partial \theta_x^{(1)}}{\partial x}, \\
 \epsilon_{yy}^{(1)} &= \frac{\partial v^{(1)}}{\partial y} = \frac{\partial v_o}{\partial y} - \psi \frac{\partial \theta_y^{(2)}}{\partial y} + \psi^2 \frac{\partial v^*}{\partial y} - \psi^3 \frac{\partial \theta_y^*}{\partial y} + (z + \psi) \frac{\partial \theta_y^{(1)}}{\partial y}, \\
 \epsilon_{xy}^{(1)} &= \frac{\partial u^{(1)}}{\partial y} + \frac{\partial v^{(1)}}{\partial x} = \left(\frac{\partial u_o}{\partial y} + \frac{\partial v_o}{\partial x} \right) - \psi \left(\frac{\partial \theta_x^{(2)}}{\partial y} + \frac{\partial \theta_y^{(2)}}{\partial x} \right) + \psi^2 \left(\frac{\partial u^*}{\partial y} + \frac{\partial v^*}{\partial x} \right) \\
 &\quad - \psi^3 \left(\frac{\partial \theta_x^*}{\partial y} + \frac{\partial \theta_y^*}{\partial x} \right) + (z + \psi) \left(\frac{\partial \theta_x^{(1)}}{\partial y} + \frac{\partial \theta_y^{(1)}}{\partial x} \right).
 \end{aligned} \tag{12}$$

$$\begin{aligned}
 \gamma_{xz}^{(1)} &= \frac{\partial w^{(1)}}{\partial x} + \frac{\partial u^{(1)}}{\partial z} = \left(\frac{\partial w_o}{\partial x} + \theta_x^{(1)} \right), \\
 \gamma_{yz}^{(1)} &= \frac{\partial w^{(1)}}{\partial y} + \frac{\partial v^{(1)}}{\partial z} = \left(\frac{\partial w_o}{\partial y} + \theta_y^{(1)} \right).
 \end{aligned}$$

$$\begin{aligned}
 \epsilon_{xx}^{(2)} &= \frac{\partial u^{(2)}}{\partial x} = \frac{\partial u_o}{\partial x} + z \frac{\partial \theta_x^{(2)}}{\partial x} + z^2 \frac{\partial u^*}{\partial x} + z^3 \frac{\partial \theta_x^*}{\partial x}, \\
 \epsilon_{yy}^{(2)} &= \frac{\partial v^{(2)}}{\partial x} = \frac{\partial v_o}{\partial y} + z \frac{\partial \theta_y^{(2)}}{\partial y} + z^2 \frac{\partial v^*}{\partial y} + z^3 \frac{\partial \theta_y^*}{\partial y}, \\
 \epsilon_{xy}^{(2)} &= \frac{\partial u^{(2)}}{\partial y} + \frac{\partial v^{(2)}}{\partial x} = \left(\frac{\partial u_o}{\partial y} + \frac{\partial v_o}{\partial x} \right) + z \left(\frac{\partial \theta_x^{(2)}}{\partial y} + \frac{\partial \theta_y^{(2)}}{\partial x} \right) \\
 &\quad + z^2 \left(\frac{\partial u^*}{\partial y} + \frac{\partial v^*}{\partial x} \right) + z^3 \left(\frac{\partial \theta_x^*}{\partial y} + \frac{\partial \theta_y^*}{\partial x} \right).
 \end{aligned} \tag{13}$$

$$\begin{aligned}
 \gamma_{xz}^{(2)} &= \frac{\partial w^{(2)}}{\partial x} + \frac{\partial u^{(2)}}{\partial z} = \left(\frac{\partial w_o}{\partial x} + \theta_x^{(2)} + 2z u^* + 3z^2 \theta_x^* \right), \\
 \gamma_{yz}^{(2)} &= \frac{\partial w^{(2)}}{\partial y} + \frac{\partial v^{(2)}}{\partial z} = \left(\frac{\partial w_o}{\partial y} + \theta_y^{(2)} + 2z v^* + 3z^2 \theta_y^* \right).
 \end{aligned}$$

$$\begin{aligned}
 \epsilon_{xx}^{(3)} &= \frac{\partial u^{(3)}}{\partial x} = \frac{\partial u_o}{\partial x} + \psi \frac{\partial \theta_x^{(2)}}{\partial x} + \psi^2 \frac{\partial u^*}{\partial x} + \psi^3 \frac{\partial \theta_x^*}{\partial x} + (z - \psi) \frac{\partial \theta_x^{(3)}}{\partial x}, \\
 \epsilon_{yy}^{(3)} &= \frac{\partial v^{(3)}}{\partial y} = \frac{\partial v_o}{\partial y} + \psi \frac{\partial \theta_y^{(2)}}{\partial y} + \psi^2 \frac{\partial v^*}{\partial y} + \psi^3 \frac{\partial \theta_y^*}{\partial y} + (z - \psi) \frac{\partial \theta_y^{(3)}}{\partial y}, \\
 \epsilon_{xy}^{(3)} &= \frac{\partial u^{(3)}}{\partial y} + \frac{\partial v^{(3)}}{\partial x} = \left(\frac{\partial u_o}{\partial y} + \frac{\partial v_o}{\partial x} \right) + \psi \left(\frac{\partial \theta_x^{(2)}}{\partial y} + \frac{\partial \theta_y^{(2)}}{\partial x} \right) + \psi^2 \left(\frac{\partial u^*}{\partial y} + \frac{\partial v^*}{\partial x} \right) \\
 &\quad + \psi^3 \left(\frac{\partial \theta_x^*}{\partial y} + \frac{\partial \theta_y^*}{\partial x} \right) + (z - \psi) \left(\frac{\partial \theta_x^{(3)}}{\partial y} + \frac{\partial \theta_y^{(3)}}{\partial x} \right).
 \end{aligned} \tag{14}$$

$$\gamma_{xz}^{(3)} = \frac{\partial w^{(3)}}{\partial x} + \frac{\partial u^{(3)}}{\partial z} = \left(\frac{\partial w_o}{\partial x} + \theta_x^{(3)} \right), \quad \gamma_{yz}^{(3)} = \frac{\partial w^{(3)}}{\partial y} + \frac{\partial v^{(3)}}{\partial z} = \left(\frac{\partial w_o}{\partial y} + \theta_y^{(3)} \right).$$

These relations for all the layers are quite similar, except for the 2D-FG layer, where the modulus of elasticity E is not constant as in the homogenous top and bottom layers. In 2D-FGM, the modulus of elasticity E is a function of both x and z -coordinates. The following matrix form represents the general form of normal stress-strain relations, which can be used for any layer configuration considering a constant value of Poisson's ratio ν throughout plate's geometry and plain stress assumptions.

$$\begin{bmatrix} \sigma_{xx}^{(i)} \\ \sigma_{yy}^{(i)} \\ \tau_{xy}^{(i)} \end{bmatrix} = \frac{E(x,z)}{(1-\nu^2)} \begin{bmatrix} 1 & \nu & 0 \\ \nu & 1 & 0 \\ 0 & 0 & (1-\nu)/2 \end{bmatrix} \begin{bmatrix} \epsilon_{xx}^{(i)} \\ \epsilon_{yy}^{(i)} \\ \epsilon_{xy}^{(i)} \end{bmatrix}. \quad (15)$$

$$\begin{bmatrix} \tau_{xz}^{(i)} \\ \tau_{yz}^{(i)} \end{bmatrix} = \frac{E(x,z)}{2(1+\nu)} \begin{bmatrix} 1 & 0 \\ 0 & 1 \end{bmatrix} \begin{bmatrix} \gamma_{xz}^{(i)} \\ \gamma_{yz}^{(i)} \end{bmatrix}. \quad (16)$$

After deriving the detailed constitutive relations, the next step involves FE formulation. In the present model, an 8-noded quadrilateral element will be used for the plate structure with 13-DoF per node that appears in *Eqs. (6-8)*. The shape functions associated with the 8-node element are given as:

$$\begin{aligned} N_1(\xi, \eta) &= \frac{1}{4}(1-\xi)(1-\eta)(-\xi-\eta-1), & N_5(\xi, \eta) &= \frac{1}{2}(1-\eta)(1+\xi)(1-\xi), \\ N_2(\xi, \eta) &= \frac{1}{4}(1+\xi)(1-\eta)(\xi-\eta-1), & N_6(\xi, \eta) &= \frac{1}{2}(1-\eta)(1+\eta)(1+\xi), \\ N_3(\xi, \eta) &= \frac{1}{4}(1+\xi)(1+\eta)(\xi+\eta-1), & N_7(\xi, \eta) &= \frac{1}{2}(1+\eta)(1+\xi)(1-\xi), \\ N_4(\xi, \eta) &= \frac{1}{4}(1-\xi)(1+\eta)(-\xi+\eta-1), & N_8(\xi, \eta) &= \frac{1}{2}(1-\xi)(1+\eta)(1-\eta). \end{aligned} \quad (17)$$

Where ξ and η are the natural-coordinate system defined by the element geometry, whereas N_i is the shape function associated with the i^{th} node. The total 13-DoF for the whole element can be written using the shape functions stated earlier as the summation of individual nodal displacement given as:

$$\Delta = \sum_{i=1}^8 N_i \Delta_i. \quad (18)$$

Where $[\Delta]$ is the nodal unknown vector for the 13-DoF written as:

$$[\Delta] = \left[u_o \quad v_o \quad w_o \quad \theta_x^{(2)} \quad \theta_y^{(2)} \quad u^* \quad v^* \quad \theta_x^* \quad \theta_x^* \quad \theta_x^{(1)} \quad \theta_y^{(1)} \quad \theta_x^{(3)} \quad \theta_y^{(3)} \right]^T. \quad (19)$$

The generalized strain-displacement relations can be expressed in terms of the nodal unknown vector in matrix form as:

$$\epsilon^{(i)} = [B^{(i)}][\Delta]. \quad (20)$$

Where $[B^{(i)}]$ are 13-matrices that relates strains to nodal unknown vector. The next step involves applying the principle of energy conservation, which relates energies associated with the system under consideration, i.e., strain and external work energies. To formulate the static problem, Hamilton's principle is used, which is used by many authors including Belarbi et al. [26]. Hamilton's Principle relates strain and work done by the external load of the system as:

$$\delta \Pi = \delta \int_{t_1}^{t_2} (W - U) dt. \quad (21)$$

Where U and W are the strain energy and work done by an external load, respectively. Each of these energies will be derived independently. Strain energy reflects the stiffness of the system; it is the integration of the stress-strain product integrated through plate's volume. For the three-layered plate, the strain energy is expressed as:

$$\delta U = \frac{1}{2} \left[\begin{aligned} & \int_{A_1} \int_{-(\psi+h_1)}^{\psi} \left(\sigma_{xx}^{(1)} \delta \varepsilon_{xx}^{(1)} + \sigma_{yy}^{(1)} \delta \varepsilon_{yy}^{(1)} + \sigma_{xy}^{(1)} \delta \varepsilon_{xy}^{(1)} + \tau_{xz}^{(1)} \delta \gamma_{xz}^{(1)} + \tau_{yz}^{(1)} \delta \gamma_{yz}^{(1)} \right) dV_1 \\ & + \int_{A_2} \int_{-\psi}^{\psi} \left(\sigma_{xx}^{(2)} \delta \varepsilon_{xx}^{(2)} + \sigma_{yy}^{(2)} \delta \varepsilon_{yy}^{(2)} + \sigma_{xy}^{(2)} \delta \varepsilon_{xy}^{(2)} + \tau_{xz}^{(2)} \delta \gamma_{xz}^{(2)} + \tau_{yz}^{(2)} \delta \gamma_{yz}^{(2)} \right) dV_2 \\ & + \int_{A_3} \int_{\psi}^{(\psi+h_3)} \left(\sigma_{xx}^{(3)} \delta \varepsilon_{xx}^{(3)} + \sigma_{yy}^{(3)} \delta \varepsilon_{yy}^{(3)} + \sigma_{xy}^{(3)} \delta \varepsilon_{xy}^{(3)} + \tau_{xz}^{(3)} \delta \gamma_{xz}^{(3)} + \tau_{yz}^{(3)} \delta \gamma_{yz}^{(3)} \right) dV_3 \end{aligned} \right]. \quad (22)$$

where A_1, A_2, A_3 and V_1, V_2, V_3 are the xy-plane areas and volumes for the lower, middle and upper layers, respectively. Using previously stated relations, the strain energy can be rewritten in the following matrix form

$$\delta U = \frac{1}{2} [\delta \Delta]^T \left([K^{(1)}] + [K^{(2)}] + [K^{(3)}] \right) [\Delta] = \frac{1}{2} [\delta \Delta]^T [K_{tot}] [\Delta]. \quad (23)$$

Where the total elemental stiffness matrix $[K_{tot}]$ with a matrix size of $[104 \times 104]$ is the sum of the elemental stiffness matrices for the lower, middle and upper layers. External work done by a distributed static load applied on the top surface of the plate is given by:

$$\begin{aligned} \delta W &= \int_{\Delta} \int_{\Delta} [\Delta]^T [N_i]^T [f(x,y)] dA = [\Delta]^T \int_{\Delta} [F(x,y)]_i dA, \\ [F(x,y)]_i &= [N_i]^T [f(x,y)]^T. \end{aligned} \quad (24)$$

Where $F(x,y)$ is the static load applied transversely on the top surface of the plate, whereas $f(x,y)$ is the discretized load on each nodal point. Total elemental load vector $[F(x,y)]_{tot}$ of a size $[104 \times 1]$ is calculated by adding the nodal forces for one element as

$$\begin{aligned} [F(x,y)]_{tot} &= \sum_{i=1}^8 \int_{\Delta} [N_i]^T [f(x,y)]^T dA \\ &= \sum_{i=1}^8 \int_{\Delta} [N_i]^T [0 \ 0 \ F \ 0 \ 0 \ 0 \ 0 \ 0 \ 0 \ 0 \ 0 \ 0 \ 0]^T dA. \end{aligned} \quad (25)$$

The equation of motion for the one element plate structure considering the FE model will lead to the following static equation of motion.

$$[K_{tot}] [\Delta] = [F_{tot}]. \quad (26)$$

Where $[K_{tot}]$ and $[F_{tot}]$ are the elemental stiffness matrix and force vector presented in Eq. (23) and Eq. (25), respectively, whereas $[\Delta]$ is the unknown vector. Equations of Motion are solved after imposing the boundary conditions applied to the plate structure. Each supported plate edges could be either Free (F), Simply (S), or Clamped (C). For a plate edge with simply supported conditions, the following equations are applied [26].

$$\begin{aligned} u_o = w_o = \theta_x^{(2)} = u^* = \theta_x^* = \theta_x^{(1)} = \theta_x^{(3)} = 0 & \quad \text{at} \quad y = 0, b, \\ v_o = w_o = \theta_y^{(2)} = v^* = \theta_y^* = \theta_y^{(1)} = \theta_y^{(3)} = 0 & \quad \text{at} \quad x = 0, a. \end{aligned} \quad (27)$$

However, for a plate edge with clamped supported conditions, all DoF associated with that edge are set to be zero [26].

$$u_o = v_o = w_o = \theta_x^{(2)} = \theta_y^{(2)} = u^* = v^* = \theta_x^* = \theta_y^* = \theta_x^{(1)} = \theta_y^{(1)} = \theta_x^{(3)} = \theta_y^{(3)} = 0. \quad (28)$$

The nomenclature of plate's supports is stated starting from the lower, right, upper and left edges, respectively, i.e., a plate with (SFSC) boundary conditions means that the plate is simply, free, simply and clamped supported on the lower, right, upper and left edges of the plate, respectively. Fig. 4 demonstrates various boundary conditions to be used in the current study, which are widely in the literature [27].

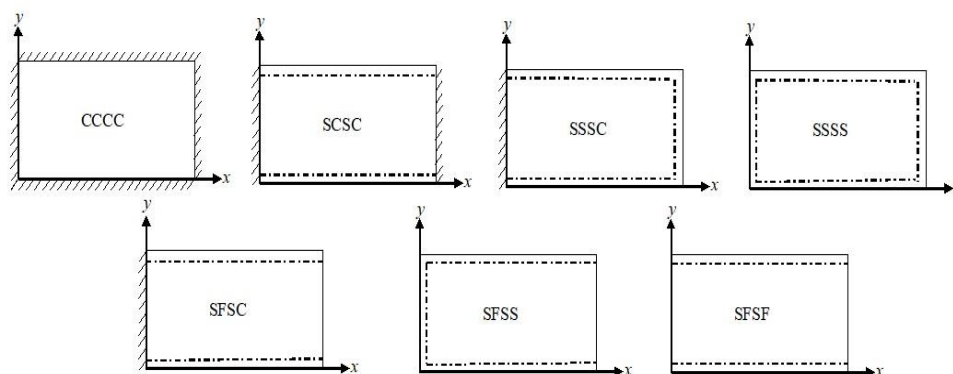


Fig. 4. Boundary conditions nomenclature.

Table 1 summarizes plate’s geometry to be investigated in the current study. The aforementioned formulations and boundary conditions will be numerically applied in the following section.

Table 1. Plate’s Geometry to be investigated.

Plate’s Width to Length Ratio b/a	Plate’s Side to Thickness Ratio a/h	Layers Thickness Ratio
1 (Square)	$a/h = 5 - 100$	1-8-1, 1-3-1, 1-2-1, 1-1-1, 0-1-0 and 2-1-2

Due to small variation in Poisson’s ratio ν for both ceramic and metallic materials, a constant value for all materials is used, i.e., 0.3. Plate’s geometry used in the current study includes only square plates ($b/a = 1$), with different plate’s side to thickness ratios ($a/h = 5-100$). Layer thickness ratio is described as three numbers describing the fraction of each layer to the total thickness of the layered plate b . For example, a thickness ratio of (1-8-1) means the lower and upper layers are (0.1 b) each, while the middle layer is (0.8 b). Seven different applied boundary conditions are used in the current study, Fig 4. Plane stress assumptions are used in this problem where the structure is considered a thin structure assuming normal stress and strains in x -direction to be zero. Bending behavior will be investigated for the layered plate where a uniformly distributed load is considered.

3 | Results and Discussions

Results obtained in this section are extracted from a computer-based program using Maple software. Results are mainly divided into two categories, two verification problems and parametric studies. The verification problems will be carried out to compare the present formulations with some special case studies presented in the literature. The first verification problem presents the determination of the plate’s central deflection of a single 1D-FG layer only. Whereas the second verification problem compares central deflection of the 1D-FG layer embedded between ceramic and metal layers. Table 2 summarizes verification problems (material properties and types of applied loads) to be verified in subsequent sections. An optimum number of elements considering both the relative approximate error and CPU elapsed time is chosen for a plate mesh grid of (6×6), hence 36 plate elements will be used in the upcoming analysis.

Table 2. Material properties and type of applied loads for verification problems 1 and 2.

Model no.	E_M [GPa]	E_C [GPa]	Poisson’s Ratio ν	Type of applied load
Verification Problem 1	70	380	0.3	Uniformly distributed static load
Verification Problem 2	70	380	0.3	Bi-sinusoidal static load

3.1 | Verification Problem 1

In this verification problem by setting $b_1 = b_3 = n_x = 0$, $b_2 = b$, $C_1 = C_2 = C$ and $M_1 = M_2 = M$ where E_C and E_M are given in Table 2. The dimensionless form for the plate's central deflection \bar{w} for 1D-FG layer is defined as [28]:

$$\bar{w} = \frac{10 w E_C h^3}{F a^4}. \quad (29)$$

Where h is the thickness of the plate, w is the central deflection of the plate, E_C is the ceramic modulus of elasticity, a is the plate length and F is the intensity of the uniform load applied on the top of the plate. Table 3 illustrates comparisons with different solutions for various types of theories and the current TSDT for various volume fraction exponents n_z starting from pure ceramic plate ($n_z = 0$), pure metallic plate ($n_z = \infty$) and several FGM combinations ($n_z = 1, 2, 3, 5, 10$). It can be observed from Table 3 good agreements between present results compared to referenced publications including Reddy's theory, generalized shear deformation theory and with the results obtained using the HSDT approach.

Table 3. Dimensionless central deflection \bar{w} for (ssss) al/al_2O_3 square plate with plate's a/h of 10.

Reference	Reddy [28]	Zenkour [29]	Bui et al. [30]	Van Do et al. [31]	Present (6×6)
Method	Reddy's theory	GSDT	HSDT	HSDT	TSDT
n_z					
Ceramic	0.4665	0.4665	0.4630	0.4659	0.4659
1	0.9421	0.9287	0.9130	0.9224	0.9273
2	1.2227	1.1940	1.2069	1.1787	1.1928
3	1.3530	1.3200	1.3596	1.2970	1.3189
5	1.4646	1.4356	1.4874	1.4055	1.4341
10	1.6054	1.5876	1.6308	1.5651	1.5856
Metal	2.5328	2.5327	2.5120	2.4968	2.5291

3.2 | Verification Problem 2

In this verification problem, the layerwise approach will be validated for the 3-layered plate structure stated previously. Pandey and Pradyumna [32], Brischetto [33], Carrera et al. [34] and Neves et al. [35] published works will be used for this purpose. The same dimensionless central plate deflection \bar{w} parameter aforementioned in Eq. (29) will be used in this verification problem. However, a bi-sinusoidal static load instead of a uniformly distributed load will be applied transversely to the plate structure. The applied load is given in the following equation.

$$F(x, y) = F \sin\left(\frac{\pi x}{a}\right) \sin\left(\frac{\pi y}{b}\right). \quad (30)$$

Validation will be carried out for a (1-8-1) square ($b/a=1$) simply supported (SSSS) plate consists of a 1D-FG layer embedded between ceramic and metal layers with various combinations of n_z and plate side to thickness ratios (a/h), Table 4. From Table 4, it is observed the good agreement between present model results compared to the published ones for various plate theories including TSDT, Equivalent Single Layer method, Carrera's Unified Formulation and Zig-Zag theory. Besides, the effect of increasing the n_z is also observed, where the dimensionless central deflection of the plate increases when increasing n_z . This phenomenon can be explained due to the proportional relation between the n_z and the increment of metallic content in the 1D-FG layer. Therefore, plate's overall stiffness becomes softer compared to the pure ceramic rigid plate.

Table 4. Dimensionless central deflection \bar{w} of a (1-8-1) (ssss) al/al2o3 square plate embedded between ceramic and metal layers.

a/h	Reference	Mesh	Method	Volume Fraction			Exponent n_z
				1	4	5	10
4	Pandey and Pradyumna [32]	8×8	TSDT	0.7636	-	-	1.2235
	Brischetto [33]	N/A	ESL	0.7629	-	1.1327	1.2232
	Carrera et al. [34]	N/A	CUF	0.7735	1.0977	-	1.2240
	Neves et al. [35]	15×15	Zig-Zag	0.7746	1.0833	1.1236	1.2183
	Present	6×6	TSDT	0.7723	1.0947	1.1348	1.2273
10	Pandey and Pradyumna [32]	8×8	TSDT	0.6323	-	-	0.8697
	Brischetto [33]	N/A	ESL	-	-	-	-
	Carrera et al. [34]	N/A	CUF	0.6337	0.8308	-	0.8743
	Neves et al. [35]	15×15	Zig-Zag	0.6357	0.8273	0.8415	0.8712
	Present	6×6	TSDT	0.6320	0.8285	0.8430	0.8734
100	Pandey and Pradyumna [32]	8×8	TSDT	0.6074	-	-	0.8076
	Brischetto [33]	N/A	ESL	0.6073	-	0.7892	0.8077
	Carrera et al. [34]	N/A	CUF	0.6072	0.7797	-	0.8077
	Neves et al. [35]	15×15	Zig-Zag	0.6087	0.7779	0.7870	0.8045
	Present	6×6	TSDT	0.5953	0.7654	0.7749	0.7938

3.3 | Parametric Studies

After verifying the current model formulations, in this section, parametric studies will be investigated for various parameters including applied boundary conditions, volume fraction exponents in both x and z -directions (n_x and n_z) and plate's side to thickness ratio a/b . These parameters will be used to study their effect on bending behavior on the 2D-FG layered plate. The same non-dimensional plate's central deflection stated earlier in Eq. (29) will be used in the upcoming analysis. Whereas non-dimensional normal and shear stresses terms that will be used are summarized in Eq. (31).

$$\bar{\sigma}_{xx} = \left(\frac{h}{a F}\right) \sigma_{xx}, \bar{\sigma}_{yy} = \left(\frac{h}{a F}\right) \sigma_{yy}, \bar{\tau}_{xy} = \left(\frac{h}{a F}\right) \tau_{xy}, \bar{\tau}_{xz} = \left(\frac{h}{a F}\right) \tau_{xz}, \bar{\tau}_{yz} = \left(\frac{h}{a F}\right) \tau_{yz}. \quad (31)$$

Where $\bar{\sigma}$, $\bar{\tau}$ are the non-dimensional normal and shear stresses parameters, respectively. The plate under investigation is made of a 2D-FG layer that consists of two ceramics (Silicon carbide [SiC], Aluminum oxide [Al₂O₃]) and two metals (Titanium Alloy [Ti-6Al-4V], Aluminum [Al]) embedded between Titanium Alloy and Silicon carbide in both lower and upper faces of the 2D-FG layer, respectively. Table 5 illustrates material constituent's properties considering a constant value of 0.3 for Poisson's ratio ν for all materials.

Table 5. The properties of material constituents for the 2d-fg layer.

Constituents	Material	Modulus of Elasticity E [GPa]	Poisson's Ratio ν
M ₁	Ti-6Al-4V	115	0.3
M ₂	Al 1100	69	0.3
C ₁	SiC	440	0.3
C ₂	Al ₂ O ₃	300	0.3

Initially, the effect of varying n_x and n_z on the plate's central deflection will be investigated. Fig. 5 illustrates the dimensionless central deflection \bar{w} of a simply supported (SSSS) plate with a side to thickness ratio a/b of five for various combinations of n_x and n_z .

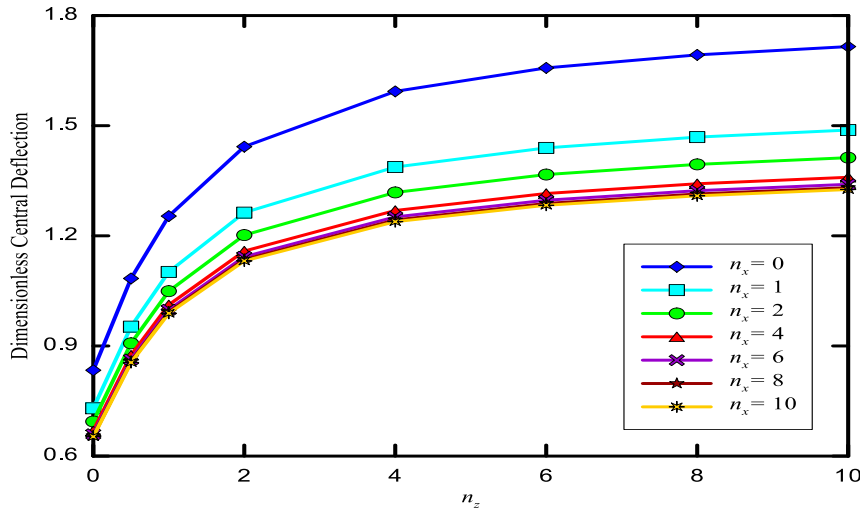


Fig. 5. Variation of non-dimensional central deflection \bar{w} for a simply supported layered plate for various volume fraction exponents n_x and n_z .

It can be observed from Fig. 5 the effect of both exponents on the plate’s deflection. It is found that as the n_z increases, the central deflection of the plate increases. This increment in plate’s deflection is associated with the increment of the metallic content as n_z increases, thus reducing the middle layer overall stiffness. On the other hand, as n_x increases, the deflection of the plate decreases, i.e., 1D-FGM ($n_x = 0$) deflects more easily compared to 2D-FGM ($n_x \neq 0$). This phenomenon is associated with high mechanical properties (modulus of elasticity) of materials C_1 and M_1 comparing to C_2 and M_2 material constituents. Therefore, as n_x increases, the middle 2D-FG layer will have a higher portion of material constituents C_1 and M_1 and less portion of materials C_2 and M_2 , thus a more rigid middle layer will be attained, which is hard to deflect comparing to a 2D-FG layer with lower n_x values. Table 6 demonstrates the numerical data illustrated in Fig. 5.

Table 6. The variation of non-dimensional central deflection \bar{w} for a simply supported layered plate for various volume fraction exponents n_x and n_z .

n_x	0	1	2	4	6	8	10
n_z							
0	0.8338	0.7302	0.6942	0.6686	0.6596	0.6553	0.6530
0.5	1.0838	0.9527	0.9072	0.8747	0.8633	0.8579	0.8549
1	1.2537	1.1018	1.0493	1.0119	0.9987	0.9924	0.9890
2	1.4428	1.2633	1.2020	1.1584	1.1430	1.1357	1.1316
4	1.5934	1.3874	1.3182	1.2690	1.2515	1.2432	1.2386
6	1.6574	1.4395	1.3669	1.3153	1.2969	1.2881	1.2833
8	1.6929	1.4689	1.3946	1.3418	1.3229	1.3140	1.3089
10	1.7155	1.4881	1.4129	1.3594	1.3403	1.3312	1.3261

The next parametric study will investigate the effect of the applied boundary conditions on the same dimensionless deflection parameter. Fig. 6 illustrates the variation of the non-dimensional central deflection parameter for a (1-8-1) square plate structure with exponent $n_x = 1$ and different combinations of n_z and applied boundary conditions.

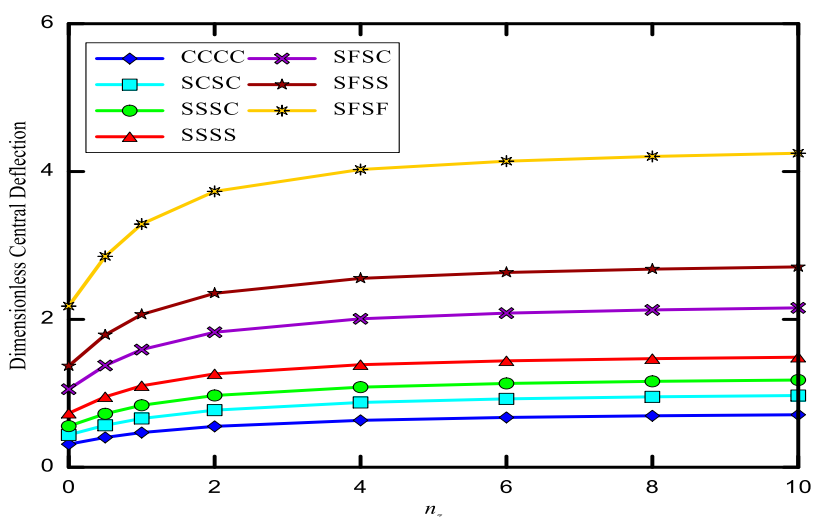


Fig. 6. Variation of non-dimensional central deflection \bar{w} for (1-8-1) layered plate with $n_x = 1$ for different values of n_z and applied boundary conditions.

From Fig. 6, the effect of n_z is observed again, whereas in this figure seven different boundary conditions were applied on the plate structure. It can be observed that the central deflection for a (CCCC) plate is less than any other applied boundary condition. Moreover, the highest plate deflection is observed for (SFSF) plate for all values n_z . Furthermore, for (SSSS) plate, the plate’s non-dimensional central deflection is between the two extreme cases, i.e., (SFSF) and (CCCC), where it can be concluded that the more constrained the plate is, less deflection is observed.

Similar procedures have been carried out to study the behavior of the plate’s central deflection for various applied boundary conditions; however, different values of n_x will be investigated instead of n_z . Fig. 7 illustrates the effect of varying exponent n_x for the seven different applied boundary conditions while maintaining a unity value for n_z . It is observed from Fig. 7 the effect of increasing n_x on the plate’s central deflection, however, this effect is hardly observed for n_x values above four. Furthermore, the effect of the applied boundary conditions is also observed for either constrained or unconstrained plate structures.

Fig. 8 illustrates the effect of the plate’s side to plate thickness ratio a/b on the plate’s central deflection. It can be observed from Fig. 8 that higher a/b ratios, i.e., thin plates, less deflection on the center of the plate are observed, i.e., the thinner the plate, less deflection is observed. However, for high a/b ratios greater than twenty, plate’s deflection remains almost constant, where the transition from thick to thin plates occurs at this ratio.

The last parameter to be investigated is the effect of the plate’s layer thickness ratios while maintaining a constant plate total thickness for all plate’s layer configurations. Plate configurations that will be examined includes ratios (1-3-1), (1-2-1), (1-1-1), (0-1-0), (2-1-2) and the previously studied plate configuration (1-8-1). The plate under investigation will be fully clamped (CCCC) plate subjected to uniformly distributed load. The middle 2D-FG layer will have a unity value for n_x and a value of five for a/b ratio, Fig. 9.

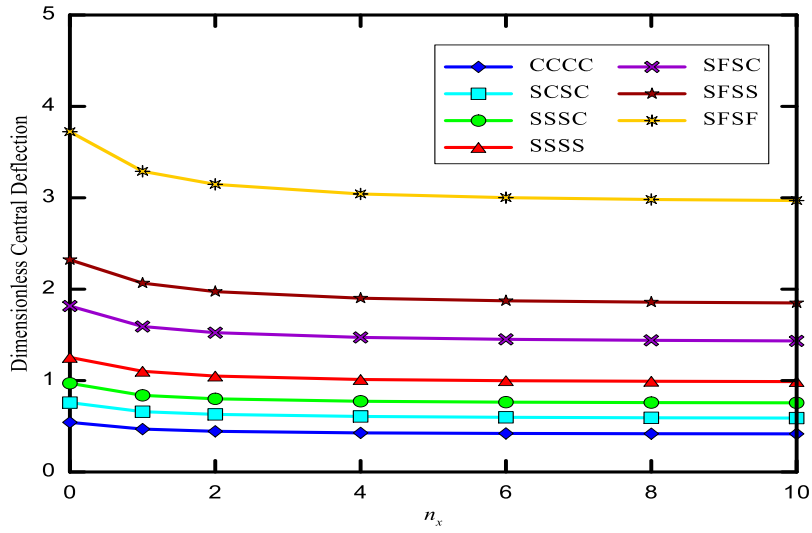


Fig. 7. Variation of non-dimensional central deflection \bar{w} for (1-8-1) layered plate with $n_z = 1$ for different values of n_x and applied boundary conditions.

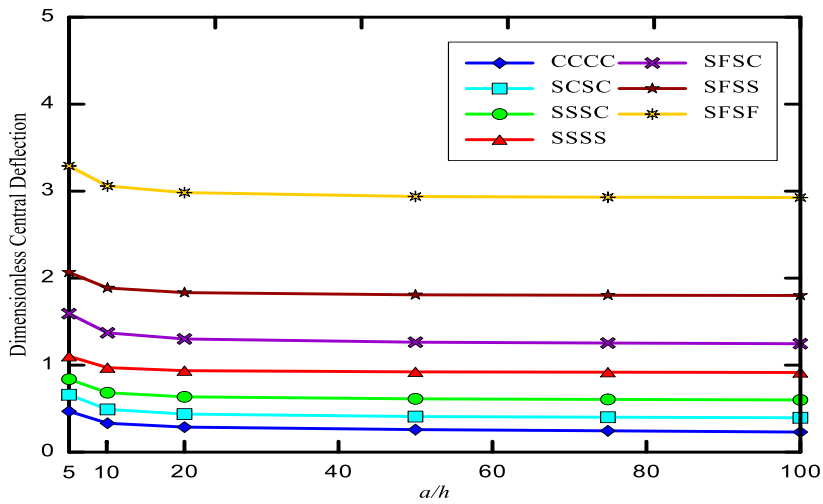


Fig. 8. Variation of non-dimensional central deflection \bar{w} for (1-8-1) layered plate with $n_x = n_z = 1$ for different values of a/h and applied boundary conditions.

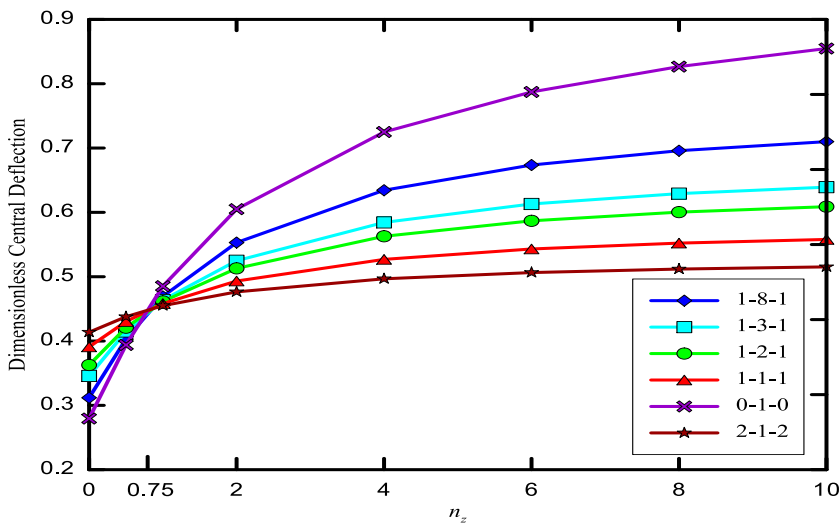


Fig. 9. Variation of non-dimensional central deflection \bar{w} for (ccc) plate with $n_x = 1$, $a/h = 5$ for different plate configurations and n_z .

It is observed from Fig. 9 that plate's central deflection also relies on the layer's thickness configurations; this relation is divided into two intervals, i.e., high ceramic and high metallic material contribution as indicated from the intersection point for all plate configurations. The first interval is related to values of n_z less than 0.75, i.e., high ceramic content, where it can be concluded that the higher the ratio of the middle 2D-FG layer compared to the upper and lower isotropic layers, less deflection is observed. This phenomenon can be explained from the high contribution of ceramic content in the whole plate structure in comparison with metallic content that is mainly located in the lower metal layer. Furthermore, as the middle 2D-FG layer ratio increases, such as (0-1-0) plate configuration, the contribution of the ceramic content in the whole plate structure will be maximum, thus a more rigid plate structure is obtained compared to low middle 2D-FG layer ratio configurations, such as (2-1-2) plate configuration. On the other hand, the second interval is related to values of n_z greater than 0.75, i.e., high metallic content, where opposite conclusions comparing to the first interval is obtained. For high values of n_z , the contribution of metallic materials inside the middle 2D-FG layer will be higher. Furthermore, the highest metallic contribution in the whole plate structure will be for high middle 2D-FG layer ratios such as (0-1-0) plate configuration. Consequently, this increment in metallic content in the overall plate structure is reflected in a softer plate structure that tends to deflect more easily compared to low middle 2D-FG layer ratios, such as (2-1-2) plate configuration.

Other than plate's deflection, it is necessary to study the effect of the volume fraction exponents n_x and n_z associated with the middle 2D-FG layer on the through-thickness stress profile for the 3-layered plate. Fig. 10 through Fig. 14 illustrate the through-thickness normal and shear stresses at the center of the plate ($x=a/2, y=b/2$). The same plate configurations used earlier will be used, a square (1-8-1) simply supported (SSSS) plate with a/b ratio of five. A unity value for the volume fraction exponent in x -direction ($n_x = 1$) and different combinations of n_z ranging from zero to six, in addition to an isotropic middle layer case ($n_x = n_z = 0$) will be also examined.

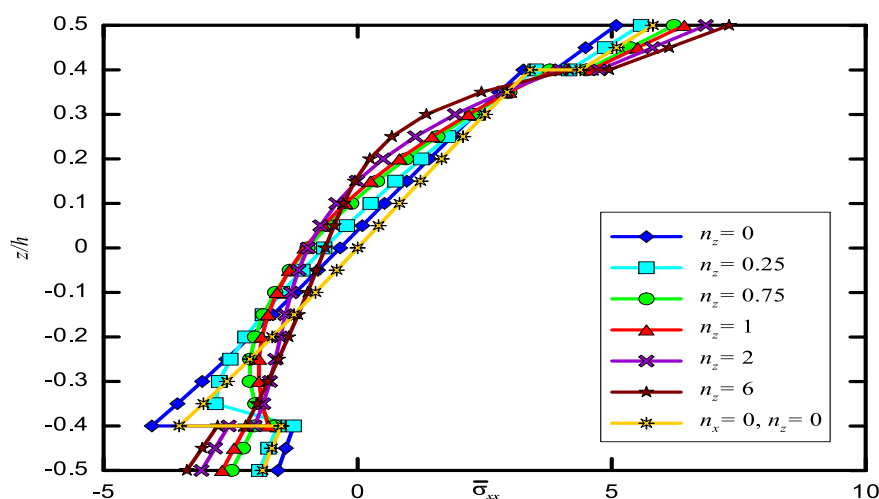


Fig. 10. Variation of non-dimensional normal stress in x-direction $\bar{\sigma}_{xx}$ for (1-8-1) simply supported plate with $n_x = 1$ and different values of n_z .

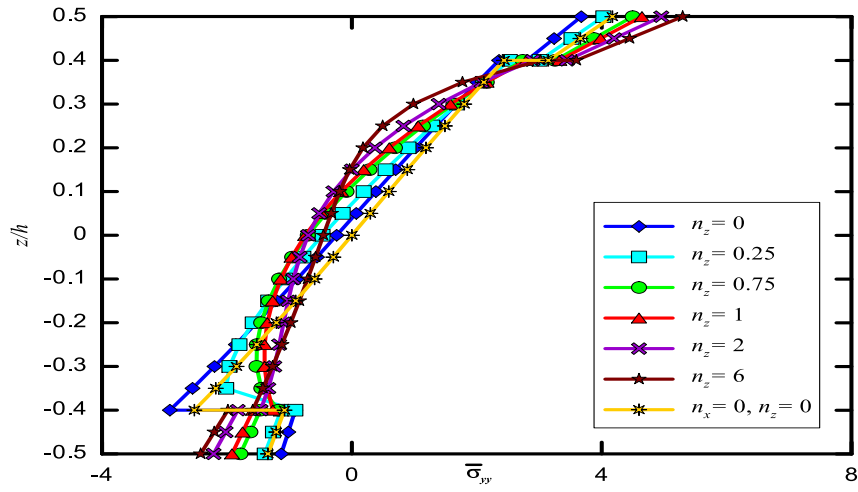


Fig. 11. Variation of non-dimensional normal stress in y-direction $\bar{\sigma}_{yy}$ for (1-8-1) simply supported plate with $n_x = 1$ and different values of n_z .

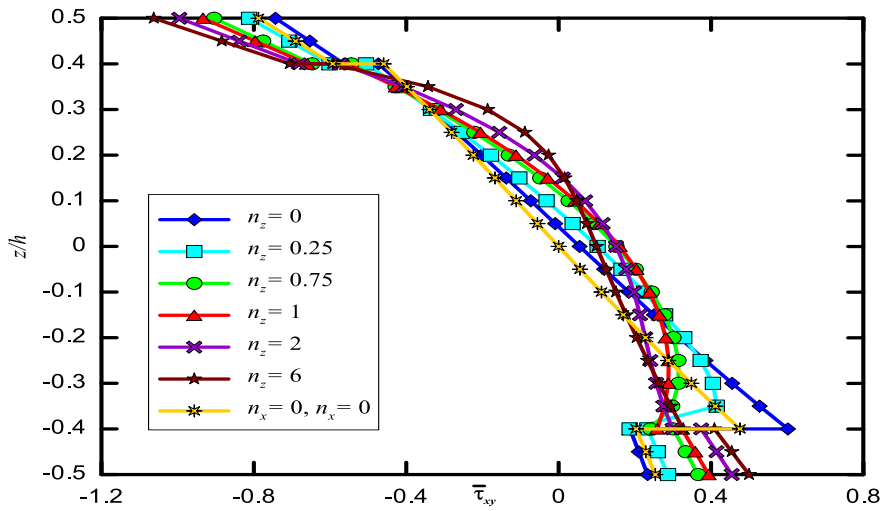


Fig. 12. Variation of non-dimensional shear stress in xy-direction $\bar{\tau}_{xy}$ for (1-8-1) simply supported plate with $n_x = 1$ and different values of n_z .

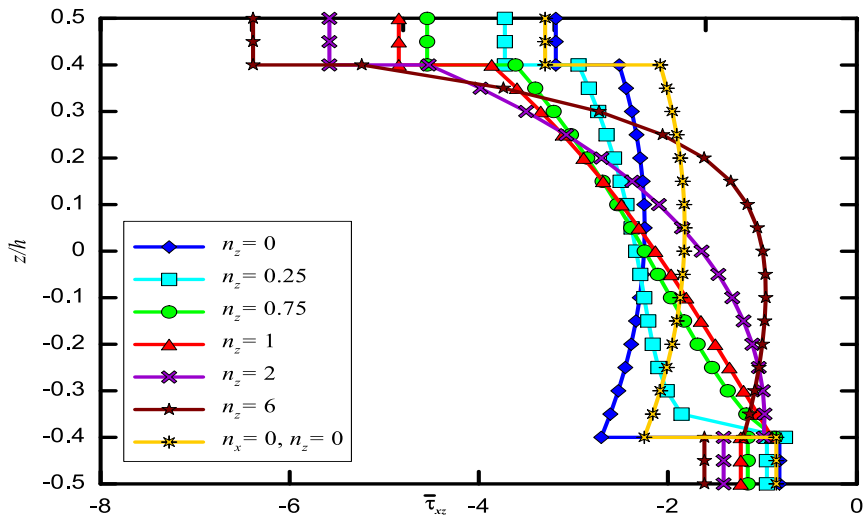


Fig. 13. Variation of non-dimensional shear stress in xz-direction $\bar{\tau}_{xz}$ for (1-8-1) simply supported plate with $n_x = 1$ and different values of n_z .

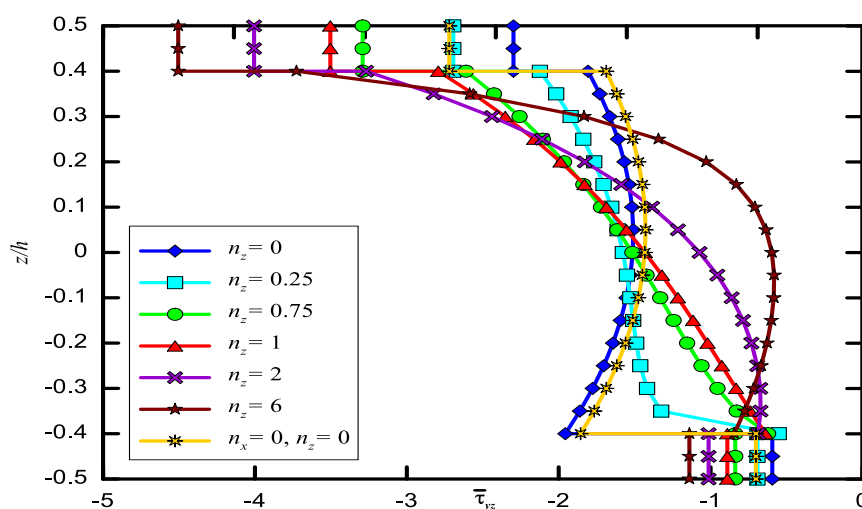


Fig. 14. Variation of non-dimensional shear stress in yz-direction $\bar{\tau}_{yz}$ for (1-8-1) simply supported plate with $n_x = 1$ and different values of n_z .

The effect of volume fraction exponents on the through-thickness normal and shear stresses are clearly shown in Fig. 10 through Fig. 14. Sharp and sudden variation of stresses across layer’s interfaces is observed for the isotropic case ($n_x = n_z = 0$), where this effect is due to sudden change in material properties at layer’s interface. Sharp peaks at the upper layer interface become smoother as n_z decreases, on the other hand, for lower layer interfaces; sharp peaks become smoother when the value of n_z increases. As n_z decreases, material properties C_1 and C_2 will contribute more than the material properties of M_1 and M_2 , where the difference between material properties at the upper layer interface becomes narrower leading to smooth stresses at the upper interface. However, as the value of n_z increases, the material properties M_1 and M_2 will contribute more than the material properties C_1 and C_2 . Thus, narrowing the gap in material properties at lower layer interface, consequently leading to smooth stresses at the lower interface.

4 | Conclusions

In this paper, the bending behavior of a rare plate model with an advanced type of material grading using an accurate enough representative element with two shear deformation theories were investigated. In addition, the current study investigated many parameters that affects the bending behavior of the layered plate structure. A layerwise FE approach for the bending analyses of a 3-layered plate consists of a 2D-FGM embedded between isotropic ceramic and metal layers were investigated. The FE approach was carried out using both FSDT for isotropic layers and TSDT for the 2D-FG layer while maintaining a continuous displacement field across the plate’s thickness using the layerwise approach.

Initially, the bending analysis verification procedure was carried out using an 8-noded quadrilateral element with 13-DoF per node. Two plate models were compared to approve the accuracy of the present formulation, i.e., single and 3-layered 1D-FGM plates. The bending analysis was investigated mainly for the plate’s central deflection. Various parametric studies were carried out to study the effect of the volume fraction exponents in longitudinal and thickness directions. Furthermore, plate’s side to thickness ratio, plate’s layer configuration and various applied boundary conditions were investigated. Formulations were executed by constructing a computer-based program using Maple Software. From the obtained results, several important conclusions can be summarized as follows:

- The volume fraction exponent in the thickness direction is proportional to the plate’s central deflection. On the other hand, as the exponent in the longitudinal direction increases the deflection of the plate decreases.
- Less deflection is observed for high a/h ratios up to 20, where above this value the deflection remains almost constant due to the transition from thick to thin plates.

- For the values of volume fraction exponents in thickness direction less than 0.75, less deflection is observed for the high middle layer ratio compared to both the upper and lower layers. On the other hand, for values greater than 0.75 opposite conclusions are obtained.

Several possible problems appear worth of further investigations, for instance, it is recommended to study the behavior of the present 2D-FGM plate structure with a dynamic load instead of static load, thus examining a plate model, which reflects realistic types of applications. Besides, this work can be also reproduced and validated experimentally while investigating the feasibility of using such materials commercially.

Acknowledgment

The authors would like to acknowledge and thank Prof. Naser Al-Huniti, of the Mechanical Engineering Department, University of Jordan, for his guidance providing language and proofreading support.

References

- [1] Koizumi, M. F. G. M. (1997). FGM activities in Japan. *Composites part b: engineering*, 28(1-2), 1-4. [https://doi.org/10.1016/S1359-8368\(96\)00016-9](https://doi.org/10.1016/S1359-8368(96)00016-9)
- [2] Mostefa, A. H., Merdaci, S., & Mahmoudi, N. (2017, November). An overview of functionally graded materials «FGM». *International symposium on materials and sustainable development* (pp. 267-278). Cham: Springer. https://doi.org/10.1007/978-3-319-89707-3_30
- [3] Irfan, S., & Siddiqui, F. (2019). A review of recent advancements in finite element formulation for sandwich plates. *Chinese journal of aeronautics*, 32(4), 785-798. <https://doi.org/10.1016/j.cja.2018.11.011>
- [4] Khorramabadi, M. K., Najafzadeh, M. M., Shahraki, J. A., & Khazaeinejad, P. (2008). Effect of shear theories on free vibration of functionally graded plates. *World academy of science, engineering and technology*, 48(2), 216-221.
- [5] Singha, M. K., Prakash, T., & Ganapathi, M. (2011). Finite element analysis of functionally graded plates under transverse load. *Finite elements in analysis and design*, 47(4), 453-460. <https://doi.org/10.1016/j.finel.2010.12.001>
- [6] Moita, J. S., Correia, V. F., Soares, C. M. M., & Herskovits, J. (2019). Higher-order finite element models for the static linear and nonlinear behaviour of functionally graded material plate-shell structures. *Composite structures*, 212, 465-475. <https://doi.org/10.1016/j.compstruct.2019.01.046>
- [7] Čukanović, D., Radaković, A., Bogdanović, G., Milanović, M., Redžović, H., & Dragović, D. (2018). New shape function for the bending analysis of functionally graded plate. *Materials*, 11(12), 2381. <https://doi.org/10.3390/ma11122381>
- [8] Efraim, E. (2011). Accurate formula for determination of natural frequencies of FGM plates basing on frequencies of isotropic plates. *Procedia engineering*, 10, 242-247. <https://doi.org/10.1016/j.proeng.2011.04.043>
- [9] Thang, P. T., Nguyen, T. T., & Lee, J. (2016). Nonlinear static analysis of thin curved panels with FG coatings under combined axial compression and external pressure. *Thin-walled structures*, 107, 405-414. <https://doi.org/10.1016/j.tws.2016.06.007>
- [10] Nguyen, T. T., Nguyen, N. L., Lee, J., & Nguyen, Q. H. (2021). Analysis of non-uniform polygonal cross-sections for thin-walled functionally graded straight and curved beams. *Engineering structures*, 226, 111366. <https://doi.org/10.1016/j.engstruct.2020.111366>
- [11] Lezgy-Nazargah, M., Vidal, P., & Polit, O. (2013). An efficient finite element model for static and dynamic analyses of functionally graded piezoelectric beams. *Composite structures*, 104, 71-84. <https://doi.org/10.1016/j.compstruct.2013.04.010>
- [12] Yas, M. H., Shakeri, M., Heshmati, M., & Mohammadi, S. (2011). Layer-wise finite element analysis of functionally graded cylindrical shell under dynamic load. *Journal of mechanical science and technology*, 25(3), 597-604. <https://doi.org/10.1007/s12206-011-0116-6>
- [13] Pandey, S., & Pradyumna, S. (2015). A layerwise finite element formulation for free vibration analysis of functionally graded sandwich shells. *Composite structures*, 133, 438-450. <https://doi.org/10.1016/j.compstruct.2015.07.087>
- [14] Nikbakht, S. J. S. M. S., Salami, S. J., & Shakeri, M. (2017). Three-dimensional analysis of functionally graded plates up to yielding, using full layer-wise finite element method. *Composite structures*, 182, 99-115. <https://doi.org/10.1016/j.compstruct.2017.09.022>
- [15] Kurtaran, H. (2014). Shape effect on free vibration of functionally graded plates. *International journal of engineering and applied sciences*, 6(4), 52-67. <https://doi.org/10.24107/ijeas.251237>

- [16] Martínez-Pañeda, E. (2019). On the finite element implementation of functionally graded materials. *Materials*, 12(2), 287. <https://doi.org/10.3390/ma12020287>
- [17] Al-Hawamdeh, O., Abu-Alshaikh, I., & Al-Hunuti, N. (2017). Finite element coding of functionally graded beams under various boundary and loading conditions. *Journal of applied research on industrial engineering*, 4(4), 279-290.
- [18] Hedia, H. S. (2005). Comparison of one-dimensional and two-dimensional functionally graded materials for the backing shell of the cemented acetabular cup. *Journal of biomedical materials research part b: applied biomaterials: an official journal of the society for biomaterials, the japanese society for biomaterials, and the australian society for biomaterials and the korean society for biomaterials*, 74(2), 732-739. <https://doi.org/10.1002/jbm.b.30258>
- [19] Nemat-Alla, M. (2003). Reduction of thermal stresses by developing two-dimensional functionally graded materials. *International journal of solids and structures*, 40(26), 7339-7356. <https://doi.org/10.1016/j.ijsostr.2003.08.017>
- [20] Joshi, K., & Kar, V. (2020). Bending analysis of bi-dimensional functionally graded plate using FEA. *Materials today: proceedings*, 26(2), 1766-1770. <https://doi.org/10.1016/j.matpr.2020.02.371>
- [21] Asemi, K., Salehi, M., & Akhlaghi, M. (2013). Three dimensional static analysis of two dimensional functionally graded plates. *International journal of recent advances in mechanical engineering (IJMECH)*, 2(2), 21-32.
- [22] Nguyen, T. T., & Lee, J. (2018). Flexural-torsional vibration and buckling of thin-walled bi-directional functionally graded beams. *Composites part b: engineering*, 154, 351-362. <https://doi.org/10.1016/j.compositesb.2018.08.069>
- [23] Nguyen, T. T., & Lee, J. (2018). Interactive geometric interpretation and static analysis of thin-walled bi-directional functionally graded beams. *Composite structures*, 191, 1-11. <https://doi.org/10.1016/j.compstruct.2018.01.064>
- [24] Lezgy-Nazargah, M. (2015). Fully coupled thermo-mechanical analysis of bi-directional FGM beams using NURBS isogeometric finite element approach. *Aerospace science and technology*, 45, 154-164. <https://doi.org/10.1016/j.ast.2015.05.006>
- [25] Lezgy-Nazargah, M., & Meshkani, Z. (2018). An efficient partial mixed finite element model for static and free vibration analyses of FGM plates rested on two-parameter elastic foundations. *Structural engineering and mechanics*, 66(5), 665-676. DOI: <http://dx.doi.org/10.12989/sem.2018.66.5.665>
- [26] Belarbi, M. O., Tati, A., & Khechai, A. (2015). Efficient layerwise finite element model for multilayer sandwich plates analysis. *Design and modeling of mechanical systems-II* (pp. 305-314). Cham: Springer. https://doi.org/10.1007/978-3-319-17527-0_30
- [27] Van Long, N., Quoc, T. H., & Tu, T. M. (2016). Bending and free vibration analysis of functionally graded plates using new eight-unknown shear deformation theory by finite-element method. *International journal of advanced structural engineering*, 8(4), 391-399. <https://doi.org/10.1007/s40091-016-0140-y>
- [28] Reddy, J. N. (2000). Analysis of functionally graded plates. *International journal for numerical methods in engineering*, 47(1-3), 663-684. [https://doi.org/10.1002/\(SICI\)1097-0207\(2000110/30\)47:1/3<663::AID-NME787>3.0.CO;2-8](https://doi.org/10.1002/(SICI)1097-0207(2000110/30)47:1/3<663::AID-NME787>3.0.CO;2-8)
- [29] Zenkour, A. M. (2006). Generalized shear deformation theory for bending analysis of functionally graded plates. *Applied mathematical modelling*, 30(1), 67-84. <https://doi.org/10.1016/j.apm.2005.03.009>
- [30] Bui, T. Q., Van Do, T., Ton, L. H. T., Doan, D. H., Tanaka, S., Pham, D. T., ... & Hirose, S. (2016). On the high temperature mechanical behaviors analysis of heated functionally graded plates using FEM and a new third-order shear deformation plate theory. *Composites part b: engineering*, 92, 218-241. <https://doi.org/10.1016/j.compositesb.2016.02.048>
- [31] Van Do, T., Nguyen, D. K., Duc, N. D., Doan, D. H., & Bui, T. Q. (2017). Analysis of bi-directional functionally graded plates by FEM and a new third-order shear deformation plate theory. *Thin-walled structures*, 119, 687-699. <https://doi.org/10.1016/j.tws.2017.07.022>
- [32] Pandey, S., & Pradyumna, S. (2018). Analysis of functionally graded sandwich plates using a higher-order layerwise theory. *Composites part b: engineering*, 153, 325-336. <https://doi.org/10.1016/j.compositesb.2018.08.121>
- [33] Brischetto, S. (2009). Classical and mixed advanced models for sandwich plates embedding functionally graded cores. *Journal of mechanics of materials and structures*, 4(1), 13-33.
- [34] Carrera, E., Brischetto, S., Cinefra, M., & Soave, M. (2011). Effects of thickness stretching in functionally graded plates and shells. *Composites part b: engineering*, 42(2), 123-133. <https://doi.org/10.1016/j.compositesb.2010.10.005>
- [35] Neves, A. M. A., Ferreira, A. J., Carrera, E., Cinefra, M., Jorge, R. M. N., & Soares, C. M. M. (2012). Static analysis of functionally graded sandwich plates according to a hyperbolic theory considering Zig-Zag and warping effects. *Advances in engineering software*, 52, 30-43. <https://doi.org/10.1016/j.advengsoft.2012.05.005>